Mirror-Coupled Plasmonic Bound States in the Continuum for Tunable Perfect Absorption

Juan Wang, Thomas Weber, Andreas Aigner, Stefan A. Maier, and Andreas Tittl*

Tailoring critical light-matter coupling is a fundamental challenge of nanophotonics, impacting fields from higher harmonic generation and energy conversion to surface-enhanced spectroscopy. Plasmonic perfect absorbers (PAs), where resonant antennas couple to their mirror images in adjacent metal films, excel at obtaining different coupling regimes by tuning the antenna-film gap size. However, practical PA applications require constant gap size, making it impossible to maintain critical coupling beyond singular wavelengths. Here, a new approach for plasmonic PAs is introduced by combining mirror-coupled resonances with the unique loss engineering capabilities of plasmonic quasi-bound states in the continuum. This novel combination allows to tailor the light–matter interaction within the under-coupling, over-coupling, and critical coupling regimes using flexible tuning knobs including asymmetry parameter, dielectric gap, and geometrical scaling factor. The study demonstrates a pixelated PA metasurface with optimal absorption over a broad range of mid-infrared wavenumbers (950–2000 cm^{-1}) using only a single gap size and applies it for multispectral surface-enhanced molecular spectroscopy. Moreover, the asymmetry parameter enables convenient adjustment of the quality factor and resonance amplitude. This concept expands the capabilities and flexibility of traditional gap-tuned PAs, opening new perspectives for miniaturized sensing platforms towards on-chip and in situ detection.

J. Wang, T. Weber, A. Aigner, S. A. Maier, A. Tittl
Chair in Hybrid Nanosystems
Nanoinstitute Munich
Faculty of Physics
Ludwig-Maximilians-Universität München
80539 München, Germany
E-mail: andreas.tittl@physik.uni-muenchen.de
S. A. Maier
School of Physics and Astronomy
Monash University
Clayton, Victoria 3800, Australia
S. A. Maier
The Blackett Laboratory
Department of Physics
Imperial College London
London SW7 2AZ, UK

1. Introduction

Metamaterials have attracted intensive attention in many fields such as holography,[1–3] energy conversion,[4–6] lasers,[7,8] biomedical imaging and diagnosis,[9–11] lightweight augmented reality and virtual reality headsets, and others,[12–14] due to their capabilities of control over light in miniaturized optical devices with tunable resonances, programmable phases and enhanced near fields. One landmark metamaterial concept for tailoring light-matter coupling is the plasmonic perfect absorber (PA), where the precise interference between a resonant antenna and its own mirror image in a neighboring metal layer separated by a dielectric spacer is leveraged to provide tunable resonances and near-unity absorbance. These advantages have led to the broad adoption of PAs for diverse applications including sensitive detectors,[15] energy harvesting,[6,16,17] thermal emitters,[18] and molecular sensing.[19–23] In general, plasmonic PAs are affected by the intrinsic losses inherent to their metallic components, limiting the quality (Q) factors of resonances, defined as the resonance position divided by the full width at half maximum (FWHM) intensity. Recently, the use of magnetic Mie resonances supported by low-loss dielectric materials coupled to metallic films has been proposed to produce resonances with high Q factors.[24] However, such magnetic resonances confine electromagnetic energy (and therefore the electromagnetic near fields) mostly inside of the all-dielectric resonators, leading to significant drawbacks for the enhancement of surface-driven coupling processes like sensing or photocatalysis, where the target system is placed adjacent to the metasurface.[25] Consequently, it remains challenging to engineer a PA geometry that simultaneously supports high Q factors, strongly enhanced and surface-confined near fields, and precisely controlled light–matter coupling. In particular, practical point-of-care spectroscopy devices in biomedical assays require optimal analyte sensitivity and high specificity over a broad wavelength range to identify and quantify target molecules. Toward this goal, different configurations of PAs were designed and demonstrated for sensing applications.[21,26,27] The main design principles of metallic PAs include surface lattice resonances (SLRs),[26] gap-induced plasmons,[23] and metal–insulator–metal (MIM) stacks.[28,29] PAs

ADVANCED
SCIENCE NEWS

www.advancedsciencenews.com

LASER
& PHOTONICS
REVIEWS

www.lpr-journal.org

based on SLRs[26,30,31] and vertical gap-induced plasmons[23,32] have achieved sharp resonances with Q factors of typically 100 in the visible spectral region, but tuning the resonances over a wide spectral range with near-unity absorbance is still challenging. To date, there are only a few reports of metallic PAs with sharp resonances in the mid-infrared (mid-IR) regime, even though they are crucial for surface-enhanced infrared absorbance spectroscopy (SEIRAS) to fingerprint molecules with high specificity compared to refractometric sensing in the visible regime.[33,34] Similarly, PAs with MIM configurations have been widely explored for near-unity absorbance from the visible to the microwave regime,[28,35–37] but the Q factors of such resonant systems are generally low on the order of 10. In addition, to identify different molecular species with spectrally separated characteristic vibrational bands, PAs based on MIM structures lack the flexibility to tailor multiple resonances over a broad IR spectral range with near-unity absorbance and high Q factors simultaneously. Dual-resonant PAs for molecular fingerprinting have been demonstrated using symmetric[21] and asymmetric crossed bars,[33] as well as single disks,[38] but still struggle to resolve vibrational bands over a broad spectral range, which is essential to, e.g., resolve complex mixtures of molecules.

To obtain critical light–matter coupling with plasmonic PAs based on MIM structures, controlling and matching the radiative loss channel to the intrinsic loss of the system is crucial, which is mainly implemented through the thickness of the insulator layer.[33,39,40] Harnessing the insulator thickness as the only tuning parameter for controlling the radiative loss makes it extremely difficult to maintain optimum coupling, unity absorbance, and high Q resonances over a broad spectral range. To overcome this limitation, a new degree of freedom for controlling the radiative loss channel is needed. As a promising candidate, photonic bound states in the continuum (BICs) have recently been introduced as a new class of resonant states that cannot couple to the far field and can therefore exhibit infinite radiative Q factors and enhanced electromagnetic near fields.[41–43] In practice, small parameter changes (geometric or excitation conditions) can perturb the BIC, leading to the emergence of quasi-BICs (qBICs) that are accessible from the far field and can be utilized to tailor light–matter interactions.[44,45]

Here, we demonstrate a new concept for engineering the optical response of metallic PAs in the mid-IR spectral range by leveraging a MIM structure composed of a resonant plasmonic qBIC metasurface, a dielectric spacer layer with constant gap size g, and a metallic mirror. Our qBIC PA scheme provides two degrees of freedom to control the radiative loss channel, where both the thickness of the insulator layer and asymmetry parameter of the meta-atoms can be used to tune the losses in the system. Significantly, at a given constant gap g, the in-plane tilting angle θ of the meta-atoms can be used to freely vary the radiative loss, allowing to reach the critical coupling (CC) conditions under any gaps at will. This 2D parameter space (g, θ) allows us to freely select between either highly enhanced electric or magnetic fields while maintaining the CC condition or to maximize the value of the total Q factor for given asymmetries. This is a crucial departure from established PA concepts, where the optical response is generally defined by the choice of the insulator layer thickness which limits spectral tunability.[46] Our design achieves a high Q factor up to 80 in simulation (≈45 in exper-

iments), addressing the limitations of inherent metal loss and demonstrating substantially larger values of Q factors compared to conventional metallic PAs. Meanwhile, the enhanced near-field intensities ($|\mathbf{E}|^2/|\mathbf{E}_0|^2$) of our plasmonic qBIC PA approach are significantly larger (>10^4) in comparison with low-loss all-dielectric metasurfaces (≈10^3).[47] The significantly higher field intensities in our plasmonic metasurface underline the fundamental resonance difference to conventional low-loss dielectric metasurfaces. Furthermore, low-loss dielectric metasurfaces do not allow tailoring of the coupling regime due to the absence of intrinsic losses within the resonators. By simultaneously tailoring both the scaling (S) factors of the meta-atoms and the asymmetric parameter (α, $\alpha = \sin\theta$) with a fixed gap, we further demonstrate a pixelated qBIC PA metasurface sensor with discrete resonances in the mid-IR, showing high spectral resolution, molecular specificity, and uniform sensitivity for SEIRAS over a broad spectral range.

2. Results and Discussion

2.1. Principle and Numerical Design of the Plasmonic qBIC PA

The qBIC PA consists of a periodic array of tilted ellipse pairs separated from a gold (Au) ground plane by a dielectric spacer layer of calcium fluoride (CaF_2) as shown in **Figure 1**a. The polarization of the illuminated incident light is along the short axis of ellipses and the incident light propagation is perpendicular to the metasurfaces. For our subsequent analysis, the crucial structural parameters of this arrangement are the tilting angle θ of the ellipses, which controls the asymmetry characteristics of the plasmonic qBIC mode, and the thickness g of the dielectric layer, determining the interaction between the plasmonic qBIC and induced mirror resonance. To obtain a qBIC PA design with the desired resonance wavelength and mode structure, we numerically optimized the geometric parameters of a unit cell including the periodicities in both x and y direction ($P_{x,0}$, $P_{y,0}$), the long/short axis of ellipses (A_0, B_0), and the height of ellipses (h). Once a suitable design for a specific wavelength is obtained, a universal scaling approach is implemented to produce resonances in other spectral regions at will through scaling of the unit cell geometry by a factor S (Figure S1, Supporting Information). As mentioned before, conventional PAs based on MIM structures mostly rely on tuning the gap size g.[37,40] This established tuning process is maintained in our design; however, our PA concept incorporating plasmonic qBICs creates a new degree of freedom for tailoring the absorption enhancement and coupling regime, significantly expanding current capabilities by leveraging the precise control over radiative loss channels provided by the asymmetric parameter α of the metasurface layer (Figure 1a) and polarization selectivity (Figure S12, Supporting Information).

Our numerical simulations of the current density at resonance (for details see Experimental Section) show clear plasmonic qBIC and induced mirror qBIC modes with anti-parallel circulating currents and associated magnetic dipole moments (Figure 1b). The current flow in the tilted metallic ellipse pairs shows a characteristic anti-parallel behavior associated with BIC-like based unit cells, which was previously observed in the dipolar displacement currents of all-dielectric qBIC metasurfaces.[47] The emergence of this distinct mode in the proposed MIM structure indicates
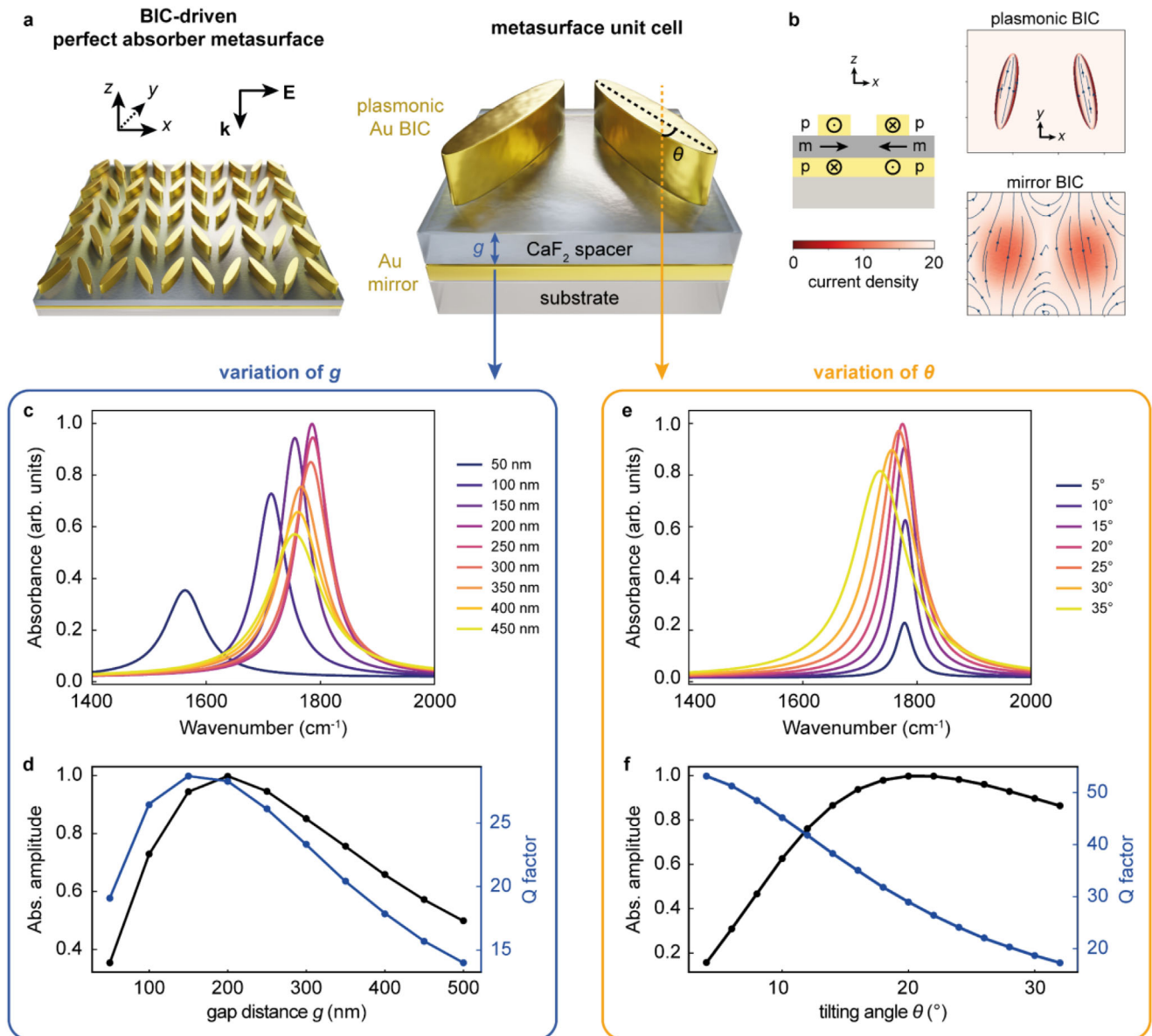
Figure 1. Operating principle and schematic of the plasmonic qBIC PA concept. a) Metasurface overview and close-up diagram of a unit cell of a PA platform consisted of paired tilting ellipses and an Au ground plane separated by a dielectric CaF_2 layer. The gap size (g) associated with the dielectric spacer and the asymmetric parameter (θ) of ellipse are highlighted. b) Side-view of a unit cell indicating the current flow and induced magnetic dipole responses, and current density map of the plasmonic and mirror qBICs. c) Absorbance spectra of a qBIC PA with constant $\theta = 20°$ and varying g. d) Extracted absorbance amplitudes and Q factors for the system with varying g at a constant $\theta = 20°$. e) Absorbance spectra of a qBIC PA with constant $g = 200$ nm and varying θ. f) Extracted absorbance amplitudes and Q factors for the system with varying θ for a gap of g = 200 nm. A scaling factor of S = 1 is used in (c) and (e).

that the nature of the qBIC mode associated with the tilted ellipse pairs is maintained within the full qBIC PA structure. Based on the definition of the absorbance ($A = 1 - R - T$), perfect absorption requires the efficient suppression of both the reflectance (R) and transmittance (T) of the nanophotonic structure. In our design, $T = 0$ is satisfied by the presence of the optically thick Au mirror (200 nm), which prevents the incident light from penetrating through the structure. The suppression of R is achieved by tailoring the gap size (g) and the asymmetric parameter (θ), which can be understood within the framework of optical impedance matching[48] or by considering the interference between different layers.[49]

Figure 1c shows the absorbance spectra with varying gap (g) at a fixed ellipse tilting angle of $\theta = 20°$, demonstrating near-unity absorbance (>99.9%) at $g = 200$ nm and $S = 1$. Away from this optimum value of g, both the maximum absorbance and Q factor of the PA resonance decreases rapidly (Figure 1d), indicating that conventional gap tuning still plays a significant role. But importantly, in our qBIC PA concept, the magnitude and spectral location of absorption can be controlled even for a fixed

value of $g = 200$ nm by tuning the in-plane asymmetric parameter α of the meta-atoms (Figure 1e). This approach creates one more degree of freedom to tailor the radiative loss, which constitutes a significant advantage for MIM-based PAs, because the same value of g cannot normally be used to simultaneously realize resonances with both near-unity absorbance and high Q factors over a wide spectra region for real-world applications.[33,38] Figure 1d,f shows the corresponding absorbance values and Q factors in both g- and θ- tailored systems. Notably, we found that the total Q factor in the (g, θ)-tailored system shows a tunable optimal value depending on the interaction between qBIC and its mirror image in the near field (Figure S2, Supporting Information). Our approach can enable us to realize multiple PA pixels with widely different resonance wavelengths but uniform Q factors on a single substrate with constant g via geometric scaling by a factor S, compared to the established gap-tuned absorber system (Figure S3, Supporting Information). In the symmetric case $(\theta = 0°)$, the additional radiative loss channel provided by the BIC-like mode disappears, removing the coupling of the PA to the far field and leading to negligible absorbance (Figure S4a, Supporting Information), which is analogous to the ideal BIC case described previously.[50,51] However, for the symmetric case, PA operation can be recovered by modifying the geometric parameters, but this results in a conventional PA design with much lower Q factor (Figure S4b,c, Supporting Information).

2.2. Practical Realization of Plasmonic qBIC PAs

The tunability of the qBIC, enabled both by the gap size g and the ellipse tilting angle θ, opens up a full 2D parameter space for realizing perfect absorption. Optimal transfer of incident light energy to the PA structure occurs at the so-called CC condition, where the intrinsic Q factor (Q_{int}) equals the external (radiative) Q factor (Q_{rad}).[40] It is worth noting that the radiative loss rate γ_{rad} includes contributions from both the gap size associated with the spacer layer ($\gamma_{rad,g}$) and the asymmetry ($\gamma_{rad, \theta}$) of the plasmonic qBIC. We examine two representative examples of CC occurring in disparate areas of the parameter space. Figure 2a,b compares the electric (E) and magnetic (H) near-fields of PAs with a thin gap ($g = 100$ nm, and $\theta = 47°$) and a thick gap ($g = 600$ nm, and $\theta = 8°$). For the PA design with a thin dielectric gap, the H field is strongly enhanced and confined in the dielectric layer, but only a comparatively low enhancement of the E field outside the gap layer is observed (**Figure 2**a). While this field profile is typical for gap plasmon modes,[52] for large gaps (Figure 2b), the situation is reversed, showing a weaker H field in the gap, but strong E field enhancement surrounding the ellipse tips, which agrees well with the previously reported field patterns for dielectric qBIC metasurfaces without metallic mirrors.[47,51] This observation demonstrates the tunability of the resonance, transitioning from a gap plasmon mode characterized by strong coupling between the antenna and the metal film, to a more conventional qBIC mode where the metal film predominantly serves as a mirror, reflecting light back onto the antenna. Furthermore, the E and H field vector distributions for both parameter cases clearly show electric dipoles with antiparallel orientation along the long axes of the ellipses as well as circulating magnetic field loops surrounding the ellipses with similarly opposing direc-

tions (Figure 2a,b). This observation further confirms that the PA modes maintain their qBIC character even for markedly different field enhancement behavior.

To generalize our observations and provide a fundamental understanding of qBIC PAs, we map and analyze a large section of the (g, θ) parameter space with both numerical simulations (Figure 2c,d) and experimental measurements (Figure 2e,f). The simulated absorbance map reveals that for any given gap size g, there is an associated value of θ that yields the CC condition (indicated by the dashed black line) and therefore perfect absorption. This behavior is reproduced in the experimental absorption maps, which are in good qualitative agreement with numerical predictions apart from a slight offset in g. Notably, larger values of g require smaller tilting angles θ to achieve the CC condition and vice versa. According to the previous work[37,40] and the following analytical results, we assume that the intrinsic loss of the system γ_{int} remains mostly constant for changing g, we can attribute the observed CC relationship to a rebalancing of the radiative loss channels between $\gamma_{rad,g}$ and $\gamma_{rad,\theta}$. It has been shown previously that $\gamma_{rad,g}$ increases with g. Consequently, for larger values of g, the radiative loss $\gamma_{rad,g}$ dominates and a qBIC unit cell with small θ and an associated small value of $\gamma_{rad,\theta}$ has to be chosen. The same argument holds for small g, where large values of $\gamma_{rad,\theta}$ are required. In addition, these insights can be used to explain why the H field is strongly confined in the dielectric layer for smaller g, which is due to the smaller $\gamma_{rad,g}$ but larger $\gamma_{rad, \theta}$. Conversely, the E field is enhanced surrounding the ellipse tips for smaller θ because of the reduced $\gamma_{rad, \theta}$. Our results indicate that the choice of g is more influential for tailoring the strength of the magnetic mode in the system and θ is responsible for the electric field confinement governed by the plasmonic qBICs. The CC line subdivides the parameter space into the regimes of under coupling (UC), where the $\gamma_{int} > (\gamma_{rad,g} + \gamma_{rad,\theta})$ and over coupling (OC), where $\gamma_{int} < (\gamma_{rad,g} + \gamma_{rad,\theta})$. The multi-tuning capability of the qBIC PA allows to precisely target and realize a specific coupling condition (UC, CC, or OC). Since deviation from the CC condition reduces the E and H fields enhancements due to the imbalance between γ_{int} and γ_{rad} (Figure S5, Supporting Information), parameter regions close to the CC line will be chosen for the later biospectroscopy demonstrations.

Figure 2c,e shows exemplarily simulated and experimental absorbance spectra of qBIC PAs with a fixed $g = 600$ nm (simulations) and $g = 580$ nm (experiments) for varying θ. The experimental absorbance spectra agree very well with the numerical predictions, but different values of the ellipse tilting angle were required to reach the CC point, with $\theta = 8°$ in simulations, and $\theta = 15°$ in experiments. Such deviations can be explained by additional experimental losses due to the surface roughness of evaporated CaF_2 and Au films (see Experimental Section), the finite size of the metasurface array (115 μm × 115 μm), and not perfectly collimated incident light. As expected, for a given value of g, the PA absorbance spectrum with smaller θ shows a reduced resonance FWHM, resulting in high Q factors. The behavior of the Q factors over the full parameter space has been investigated by calculating them from the absorbance spectra via a fitting approach using temporal coupled mode theory (TCMT) (for details see Experimental Section). The highest Q factor of 80 can be obtained for $g = 600$ nm and $\theta = 2°$ (Figure 2d and Figure S13, Supporting Information). The Q factors extracted from the
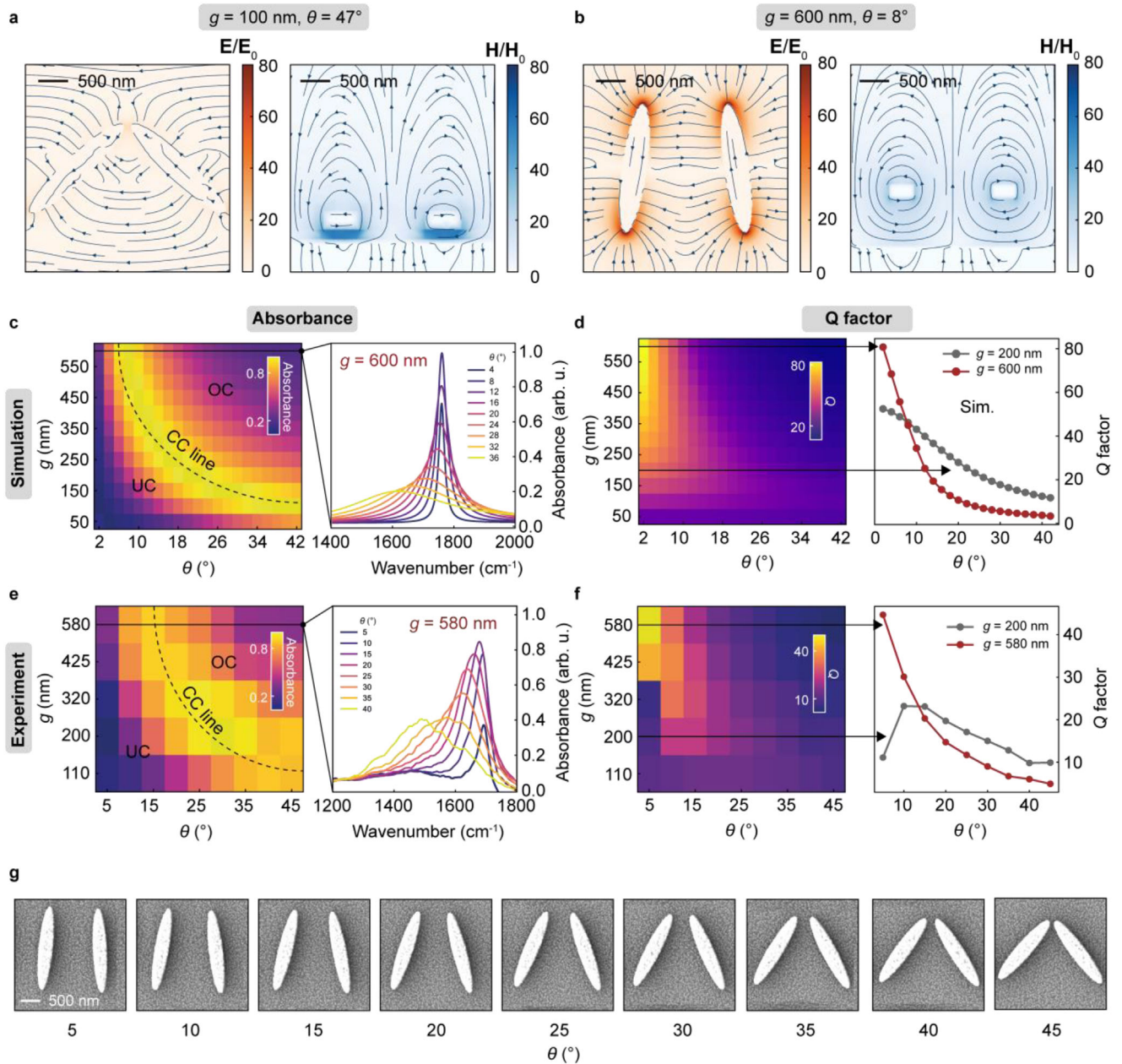
Figure 2. Tailored light-matter coupling in plasmonic qBIC PAs via simultaneous control over gap (g) and asymmetry parameter (α). a) Near-fields of a PA with $g = 100$ nm and $\theta = 47°$ at the CC condition. b) Near-fields of a PA with $g = 600$ nm, and $\theta = 8°$ at the CC condition. Orange (blue) colors indicated the E (H) field distribution in (a) and (b). c) The 2D parameter space (g, θ) map for co-tuning the light-matter coupling regime in numerical simulation and extracted numerical absorbance spectra as a function of θ with constant $g = 600$ nm. d) 2D map of calculated Q factors from each absorbance spectra in (c) and extracted Q factor plots as a function of θ with constant g (indicated by the grey and dark red lines). e) Experimental realization of 2D (g, θ) map for co-tuning the absorbance coupling regime and extracted experimental absorbance spectra as a function of θ with constant $g = 580$ nm. f) 2D Map of Q factors obtained from the measured absorbance spectra in (e) and Q factor plots with increasing θ at the fixed g (indicated by the grey and dark red lines). g) Top-view HR-SEM images that are used in panels (e) and (f) show unit cells with varying θ from 5° to 45°. Scale bar: 500 nm.

experimental measurements follow the same trend but peak at half of the simulated value (Figure 2f), which we attribute to fabrication imperfections.[53] Crucially, the maximally achievable Q factors in our new qBIC PA platform are at least four times higher than that in the conventional solely gap-tuned systems (Figure S3, Supporting Information).[40] Note that for the established conventional PA the highest Q factor is achieved at the CC

condition (Figures S3 and S4b,c, Supporting Information), while in our design, the highest Q factor is achieved in the UC regime. From the Q factor map, we can conclude that for fixed g, the Q factor decreases with increasing θ, which is mainly attributed to the increase of $\gamma_{rad, \theta}$. However, for smaller gaps ($g < 200$ nm), the Q factor does not monotonically decrease with an increase in θ, especially at the UC regime, where γ_{int} plays a dominant role,
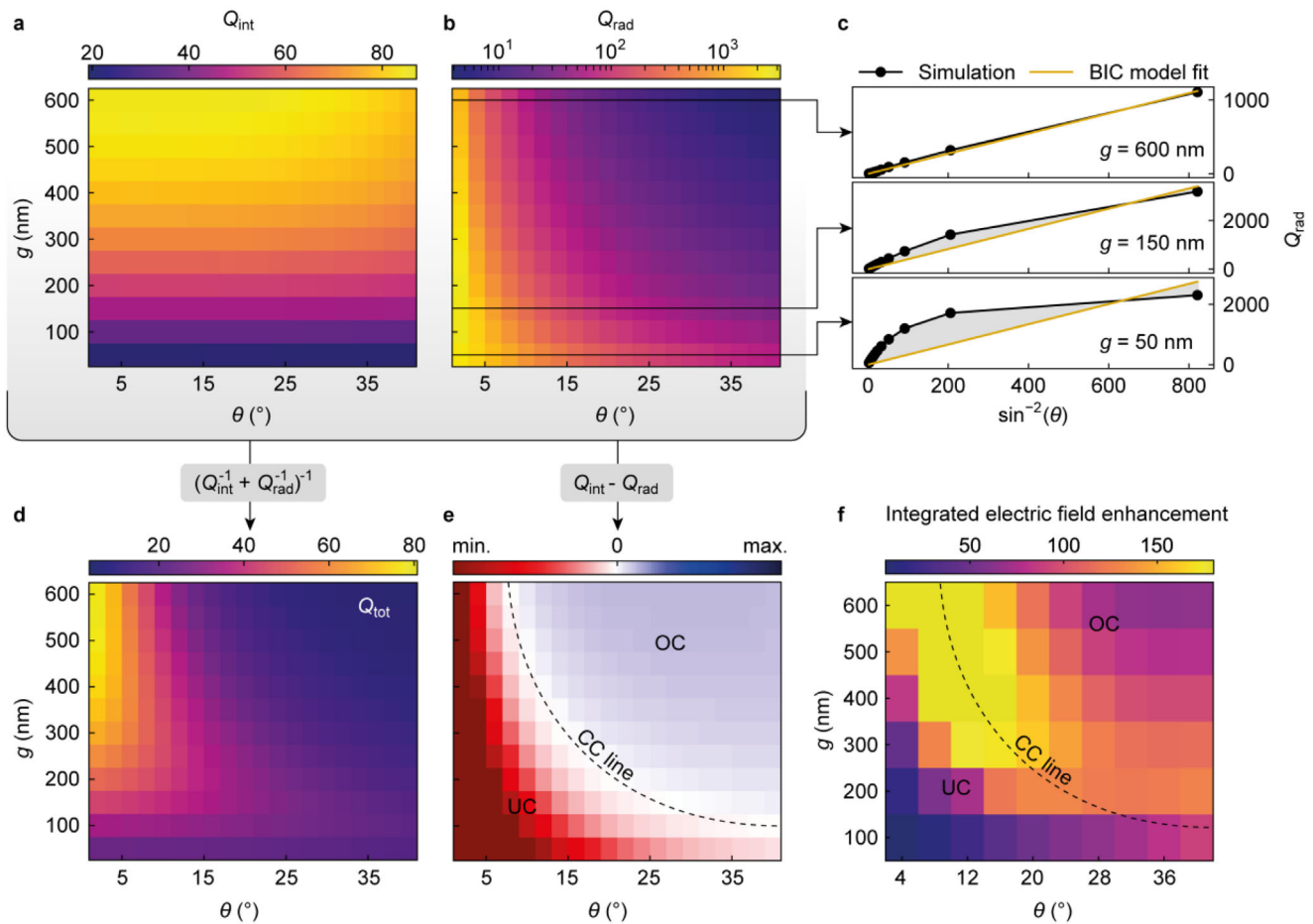
Figure 3. TCMT modelling and integrated near-field intensity enhancement evaluation of qBIC PAs. a) Q_{int} as a function of g and θ. b) Q_{rad} as a function of g and θ. c) Q_{rad} extracted from panel (b) as a function of the inverse square of the asymmetry parameter α^{-2} ($\alpha = \sin\theta$), fitted with a qBIC model. For large gaps ($g = 600$ nm), the resonance behaves like an ideal BIC, whereas smaller gap sizes lead to a deviation from the linear trend of the radiative Q factor, indicating a strong near-field interaction of the plasmonic qBIC with the mirror qBIC resonance. d) Total Q factor retrieved from panels (a) and (b). e) Map of the difference between Q_{int} and Q_{rad} as a function of g and θ. f) Integrated field intensity enhancement as a function of g and θ, where the resonance was placed approximately at 1650 cm^{-1} ($S = 1.08$).

indicating the importance of the CC condition also for these Q factors. This behavior is clearly demonstrated by the extracted Q factors plots with fixed $g = 600$ nm (580 nm) and 200 nm as a function of θ as shown in Figure 2d (simulations) and Figure 2f (experiments) and further supported by the absorbance spectra of PAs with $g = 200$ nm and varied θ in Figure S6 (Supporting Information). Importantly, these results reinforce the versatility of our concept for tailoring absorption, near fields, and Q factors of the qBIC-governed PA resonances. High-resolution scanning electronic microscope (HR-SEM) images (Figure 2g) show the fabricated unit cells of PA metasurface with varied θ used in the above measurements (for details of PA metasurface fabrication see Experimental Section).

2.3. Analytical Coupling Analysis and Near-Field Enhancement Evaluation

The plasmonic qBIC PA system has been further analyzed using TCMT,[54] allowing us to separate the contributions of the intrin-

sic and radiative Q factors to the enhanced absorption (for details see Experimental Section). For numerical analysis, we fixed the intrinsic damping rate (γ_{int}) for varying ellipse tilting angles θ, because the BIC asymmetry factor solely affects the radiative damping rates,[55] thus the intrinsic Q factor (Q_{int}) only changes slightly with θ, due to the shift of resonance positions, while Q_{int} increases significantly with g (**Figure 3**a). In contrast, the radiative damping rate γ_{rad} strongly depends on both g and θ. From the map of radiative Q factors (Figure 3b), Q_{rad} decreases with increasing g (for a fixed θ), particularly with larger θ, while for $\theta \leq 4°$, Q_{rad} first increases and then drops with g (Figure S7, Supporting Information). Looking at fixed values of g (indicated by the black arrows in Figure 3b), for gap sizes ($g = 600$ nm), Q_{rad} follows the characteristic qBIC inverse quadratic dependency with respect to the asymmetry factor $\sin\theta$ ($Q_{rad} \sim \sin^{-2}\theta$).[56] Decreasing g leads to a deviation from the qBIC regime, indicating strong near-field interaction between the plasmonic qBIC and the induced mirror qBIC (Figure 3c). Merging the intrinsic and radiative Q factors to a total Q factor (Figure 3d), reproduces panel (d) in Figure 2, which further corroborates the accuracy of our fitting

approach. CC in the PA occurs for $Q_{int} = Q_{rad}$ and therefore we can visualize the different coupling regimes by mapping the difference $Q_{int} - Q_{rad}$ of the two Q factors (Figure 3e). We find that the CC line reproduces the distinct behavior already observed in Figure 2c.

Importantly, along the CC line, both the Q factors and the **E** field intensity enhancements (noted as $|E|^2/|E_0|^2$) show an increase with increasing g (see Figures 2e,i and **3**e), indicating that the **E** field enhancement is mostly governed by the BIC-like behavior of the metasurface layer, which can be tuned via θ. On the other hand, from the map of Q_{int} (Figure 3a), an increase of Q_{int} with increasing g can give rise to much stronger enhanced near fields at the CC regime. Therefore, in general, the highest Q factors and largest near-fields enhancements can be obtained in a design with large g and small θ. The maximum achievable field intensity enhancements ($|E|^2/|E_0|^2$) are above 10^4 (Figure S8, Supporting Information), while simultaneously providing strong electromagnetic hot spots confined to the outside of resonators, enabling substantial enhancement of light–matter interactions. Furthermore, the integrated near-field intensity enhancements confirm that the strongest enhancements indeed follow the CC condition (Figure 3f, for calculation details, see Experimental Section). The large near fields obtained in a carefully tailored qBIC PA geometry are highly beneficial for the sensitive detection of surface-bound molecules, further strengthened by the freedom to flexibly tune the PA wavelength to overlap with the molecular fingerprints and the precise targeting of specific vibrational bands via the sharp resonances. Crucially, the accessible hot spots and Q factors of the resonances can be tailored simultaneously, providing high spectral selectivity and sensitivity. Taken together, these features make our PA platform excellently suited to serve as molecular sensors.

2.4. Pixelated qBIC PA Metasurfaces for Biomolecular Detection

Biomolecules contain a rich fingerprint of vibrational absorption bands over a wide range of wavelengths in the mid-IR. To identify and quantify the trace amounts of molecular species, carefully engineered nanophotonic platforms capable of delivering resonances targeted at specific molecular signatures with high Q factors and enhanced near fields for strongly enhanced light-matter interaction are essential. To highlight the molecular detection capability of our PA design, we evaluate the sensing performance of a PA realization with a large value of $g = 600$ nm and varied θ, covering the distinct UC ($\theta < \theta_{cc}$), CC ($\theta = \theta_{cc}$) and OC ($\theta > \theta_{cc}$) regimes. The value of $g = 600$ nm was chosen to simultaneously provide high Q factors (i.e., high spectral selectivity) and strong near fields in accordance with the analysis presented in Figure 3. We first investigate different coupling regimes using polymer-coated metasurfaces (**Figure 4**a). Figure 4b shows the simulated and experimental absorbance spectra of the PA upon coating with a thin layer of polymethylmethacrylate (PMMA). The thickness of the conformal PMMA layer is 2 nm in simulations and ≈1.5 nm in experiments as confirmed by spectral ellipsometry measurements. Clearly, upon addition of an absorbing analyte layer, an increase in the intrinsic loss of the coupled system is expected, where $\gamma_{int} \rightarrow \gamma_{int} + \gamma_\mu$, and γ_μ is the loss of absorbing analyte. Therefore, the absorbance amplitude is further decreased by the
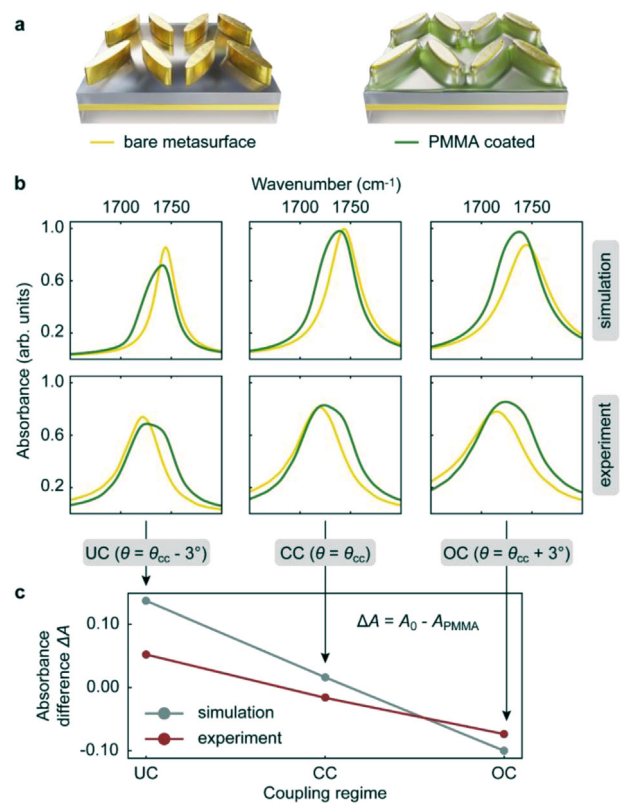

Figure 4. Coupling regimes in plasmonic qBIC PAs. a) Illustrations of bare and PMMA-coated metasurfaces. b) Simulated and experimental spectra show the absorbance modulation of PAs in the UC, CC, and OC regime when coated with a thin (2 nm in simulation and 1.5 nm in experiment) layer of PMMA polymer. c) Absorbance amplitude difference (ΔA) for different coupling regimes upon the PMMA coating compared to the bare PA.

addition of the analyte when the bare PA is in the UC regime, whereas we observe an absorbance increase in the OC regime. This behavior is attributed to an increase in γ_{int}, which drives the system closer to the CC. For the PA at the CC point, only small changes in the absorbance amplitude are expected, since the system is only shifted slightly away from the CC condition, which is reflected in both the numerical and experimental results. Figure 4c compares the change of absorbance amplitude ($\Delta A = A_{bare} - A_{sample}$) between the qBIC PA before and after analyte coating, clearly identifying the three coupling regimes based on the absorbance modulation.

To demonstrate the capability of maintaining a specific coupling regime over a wide range of mid-IR wavelengths (1250–2000 cm^{-1}), we develop a pixelated metasurface of PAs at the CC condition (**Figure 5**a), where each metapixel corresponds to a discrete frequency with near-unity absorbance (>99.4%) and high Q factors (>45) in simulations (Figures S9 and S10, Supporting Information) The full absorbance spectra of the PA pixels are shown in Figure S9 (Supporting Information). A broad wavelength coverage was achieved by linearly scaling the geometric dimensions by a factor S and simultaneously tuning the ellipse tilting angle θ (Figure 5a). The versatility of tuning θ allows to achieve the CC condition of each pixel at different wavenumbers
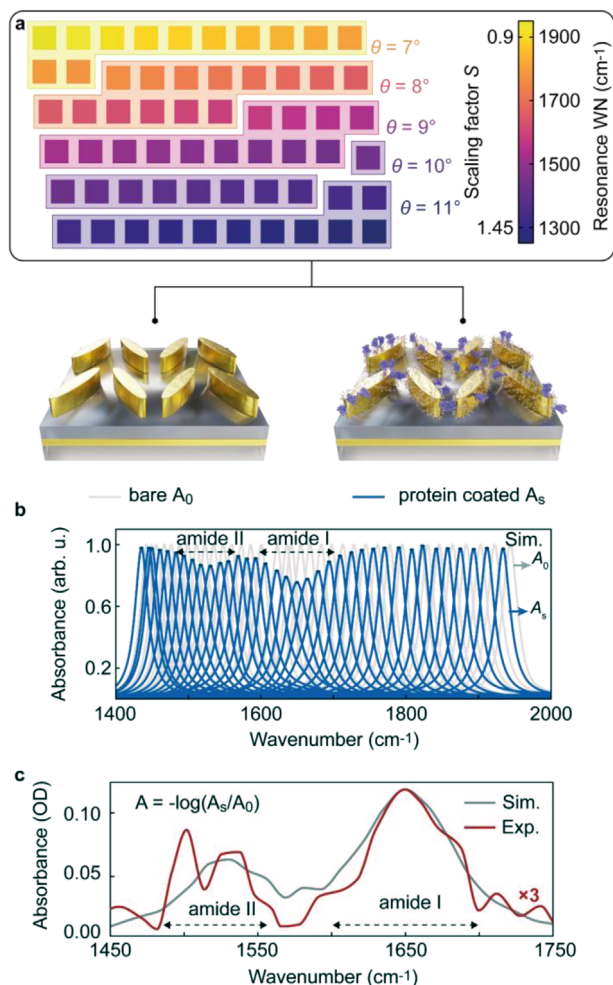
Figure 5. Pixelated plasmonic qBIC PAs for biomolecular sensing. a) A pixelated qBIC PA metasurface realizes resonances over a broad mid-IR spectral range by simultaneously controlling S and θ for a fixed gap size g = 600 nm. The corresponding θ of each metapixel is indicated and color-shadowed boxes group pixels that share the same θ. The scaling factor S of the pixels increases linearly from the top left to the bottom right of the metasurface. b) Simulated normalized absorbance spectra of the UC pixelated metasurface without molecular coating (A_0, grey color lines) and with a 2 nm thick protein coating (A_s, blue color). c) Simulated and experimental protein absorbance spectra show the characteristic amide I ($\approx$1650 cm^{-1}) and amide II ($\approx$1530 cm^{-1}) band vibrations.

while maintaining the same insulator gap. To the best of our knowledge, this is the first report of a plasmonic qBIC PA concept, where one can easily achieve a broad range of resonances with near-unity absorbance, high Q factors, strongly enhanced near fields, and precisely tailored coupling regimes (UC, CC, and OC), constituting a significant advance compared to conventional plasmonic PAs (lower Q factor and limited resonance tuning)[33,38] and film-coupled low-loss resonators (reduced field confinement/enhancement and limited control over radiative decay rates).[24]

Since the highest analyte-induced absorbance modulation change and therefore the highest molecular sensitivity is expected in the UC regime (Figure 4c), we now experimentally re-

alize a qBIC PA design for $\theta_{uc} = \theta_{cc} - 3°$. To demonstrate bi-molecular sensing, a 2 nm thick conformal protein layer was applied on top of bare PA pixels. The absorbance spectra of bare pixelated PAs (grey color, denoted as A_0) and protein-coated ones (blue color, A_s) are shown in Figure 5b. When the resonances of metapixels couple with the vibrational bands of the proteins (i.e., amide I at $\approx$1650 cm^{-1} and amide II at $\approx$1530 cm^{-1}), there is a pronounced decrease in absorbance amplitude. The IR absorbance spectrum of the protein can then be obtained from the envelopes of the respective absorbance spectra via $A = -\log(A_s/A_0)$ (Figure 5c, grey curve), reproducing the characteristic amide bands. We have evaluated the sensing performance of the pixelated PA concept using a high-affinity biotin–streptavidin binding bioassay. Biotin molecules were attached to the Au surface using an established thiolation protocol (see details in Experimental Section and Figure S11, Supporting Information). The experimentally obtained vibrational absorbance spectra of streptavidin (Figure 5c, red curve) are referenced to the signal of thiolated biotin molecules (SH-biotin), where the SH-biotin molecules serve as capture sites to specifically bind the streptavidin. The measured amide I and II vibration bands agree well with the simulation, but show a reduced absorbance amplitude, which we attribute to impurities of the gold surface and the biotin monolayer. To study the performance of molecular sensing for all coupling regimes, pixelated PAs at the CC ($\theta = \theta_{cc}$), and the OC ($\theta = \theta_{cc} + 3°$) conditions have also been realized through solely tuning the θ and compared using the biotin–streptavidin bioassay, reproducing the behavior observed for the PMMA above (Figure S11d, Supporting Information). Therefore, our qBIC PA concept shows strong promise for molecular identification over wide spectral ranges with high specificity and sensitivity, paving the way towards minimized and compact sensing platforms for biomedical assays and clinical diagnosis.

3. Conclusion

We have numerically and experimentally demonstrated a new qBIC PA metasurface concept consisting of an array of tilted ellipse pairs in an MIM configuration. Our approach allows to precisely control the radiative loss channel in the PA system through both the asymmetric parameter (α) and the insulator gap (g), delivering an additional degree of freedom for tailoring light–matter coupling and hence allowing us to precisely tailor the different light–matter coupling regimes including UC, CC, and OC over a broad spectral range. Significantly, such a qBIC PA enables multiple tuning knobs to precisely tune the coupling regimes through the in-plane ellipse tilting angle θ at any constant gap, which allows selective strong enhancement of either the electric or the magnetic fields. Crucially, we have found that the θ-induced radiative loss mainly accounts for the electric field enhancements, while the g-induced radiative loss is responsible for controlling the formation of the magnetic mode, enabling flexible resonant systems for diverse applications. Furthermore, resonances tuned to the CC regime over a broad range of mid-IR wavelengths can be achieved by both linear scaling the geometric parameters by a factor of S and tuning the tilting angle θ correspondingly, while maintaining high Q factors and near-unity absorbance (>99.4%) throughout. Tuning of the tilting angle

θ additionally allows to tune the q-factor and the resonance amplitude. Our results demonstrate that plasmonic qBIC PAs can deliver efficient light–matter coupling with the high Q factors (≈80 in simulations and ≈45 in experiments) and strongest field intensity enhancements ($\approx10^4$) found for small values of θ and large values of g, outperforming traditional PA systems. We have further demonstrated a pixelated PA metasurface with resonances in a range of 1200–2000 cm^{-1}, in different coupling regimes (UC, CC, and OC) and have applied the concept for biomolecular detection with high sensitivity and spectral selectivity. This qBIC PA concept opens a new direction toward miniaturized sensing platforms for on-chip and in situ detection and can extend to apply in energy conversion and photocatalysis. In the future, a qBIC optofluidic PA, where the analyte simultaneously acts as a spacer layer and analyte channel, which maximizes the utilization of the near-field hotspots with enhanced light-matter interaction for ultrasensitive bioassays and efficient energy conversion.

4. Experimental Section

Numerical Simulation: All numerical simulations were performed using the finite element solver contained in CST Microwave Studio 2021 (Dassault Systèmes), where periodic boundary conditions were applied and the incident light (k) was perpendicular to the metasurface plane with x-polarization (TM). Tabulated permittivity values of Au, PMMA, and protein were taken from the literature.[57–59] The refractive indices of silica glass and CaF$_2$ were assumed to be lossless with $n_{SiO2} = 1.5$ and $n_{CaF2} = 1.399$, respectively. Tuning of the PA resonances throughout the mid-IR spectral range was implemented by applying a scaling factor S to the geometric parameters ($P_{x,0}$, $P_{y,0}$, A_0, and B_0) of the unit cell (Figure S1, Supporting Information). Throughout the work, a constant Au resonator height of $h = 200$ nm was used. Besides, the conventional gap-tuned PAs consisting of brick, disk, symmetric paired ellipse arrays were simulated (see Supporting Information with more parameter details). The thickness of the conformal absorbing analyte layer was set to 2 nm in simulations. The integrated electric near-fields intensity enhancement was evaluated by the ratio between the integrated enhanced electric fields over a certain volume and the $|\mathbf{E}_0|^2$ over the same volume. This volume was defined by the periodicity in x- and y-directions and a height from the Au ground plane up to 100 nm above the top surface of the Au resonator ($H = h + g + 100$ nm).

Fabrication of qBIC PA Metasurfaces: Starting from a commercial silica glass substrate, a 200 nm thick layer of Au was first evaporated as a mirror ground plane, followed by the evaporation of a dielectric CaF$_2$ layer with varying thickness in a range of 50–600 nm. qBIC metasurface structures were fabricated on top of the layer stack by a standard electron-beam lithography process (30 kV voltage, 15 μm aperture) using a double layer of positive PMMA resist (950 K, A4, Microresist).[10] Afterward, an adhesion layer of 5 nm Ti and 200 nm of Au were deposited by electron-beam assisted evaporation, and the final metasurface structures were obtained by wet-chemical lift-off process (remover 1165, Microresist).

Optical Characterization: To characterize the optical responses of the fabricated PA metasurfaces, a mid-IR spectral imaging microscope (Spero from Daylight Solutions Inc., USA) was used for all measurements in this work. A low magnification objective (4×, NA = 0.1 with 2 mm^2 field of view) was used to ensure that large pixelated metasurfaces can be imaged simultaneously. The Spero microscope was equipped with four tunable quantum cascade lasers continuously covering the mid-IR range from 948 to 1800 cm^{-1}. A laser scanning step size of 2 cm^{-1} was used. All optical measurements were conducted in reflection mode and normalized to the reflection signal of a plain Au mirror (thickness 200 nm). To eliminate backscattering effects, the reflectance signal from an unpatterned area on the metasurface chip was collected as a reference. The final spatially resolved metasurface reflectance signals were then obtained by subtracting the reference data from the sample data. Metapixel spectra were obtained by averaging the hyperspectral reflectance data over the corresponding image pixels.

Numerical Analysis: To extract the intrinsic (γ_{int}) and radiative (γ_{rad}) damping rates of PA resonances with wavenumber υ_0, TCMT[60] was used to describe a resonator with a single port supporting reflected waves and a single resonance coupling to the far-field mediated by the coupling constant $\kappa = \sqrt{2\gamma_{rad}}$ and an intrinsic loss channel, damping the resonance with a rate γ_{int}. In this system, the absorbance (A) is given by Equation (1).

$$A = 1 - R = \frac{4\,\gamma_{rad}\,\gamma_{int}}{(\nu - \nu_0)^2 + (\gamma_{rad} + \gamma_{int})^2} \tag{1}$$

which can be directly fitted to our simulated absorbance spectra. The radiative, intrinsic, and total Q factors can then be calculated as $Q_{rad} = \frac{\upsilon_0}{2\gamma_{rad}}$, $Q_{int} = \frac{\upsilon_0}{2\gamma_{int}}$ and $Q_{tot} = \frac{\upsilon_0}{2(\gamma_{rad}+\gamma_{int})}$, respectively. To analyze the damping rates for different values of g and θ, the fact that γ_{rad} and γ_{int} are independent variables, i.e., material intrinsic losses have no effect on the radiative damping rate, by fitting absorbance spectra with different θ at a given g simultaneously with a shared value of γ_{int}, which adds stability to the fitting procedure, was used.

Molecular Sensing: For the PMMA-coated PA, a layer of 0.1 % PMMA (950 K, diluted in anisole) was spin-coated onto the bare PA (3000 rpm, 1 min), followed by a 5 min baking at 180 °C. Ellipsometric measurements (HS-190, J.A. Woollam VASE) on a clean silicon substrate coated with the same layer were used to precisely determine the thickness of the PMMA film.

For the biomolecular detection experiments, a layer of capture SH-biotin molecules (HS—(CH$_2$—CH$_2$—O)$_5$—OCH$_2$CH$_2$—NH—biotin, Prochimia Surfaces, Poland) was immobilized on the freshly prepared PA metasurfaces. The applied concentration of SH-biotin solution was 1.2 mg mL^{-1} in a degassed mixture of deionized water and ethanol with a volume ratio of 1:1. After incubation of the metasurfaces in SH-biotin solution for 4 h, the metasurface was rinsed continuously by ethanol and dried by a stream of N$_2$ flow. Then, the functionalized metasurface was incubated in streptavidin solution for 2 h by drop casting with a volume of 80 μL at room temperature, where the used concentration of streptavidin was 16 μM. After incubation, the streptavidin immobilized metasurface was rinsed by phosphate-buffered saline (PBS) buffer (1×) and dried by N$_2$ flow. After each immobilization step, the PA metasurface was transferred to the Spero mid-IR microscope for spectroscopic imaging.

Supporting Information

Supporting Information is available from the Wiley Online Library or from the author.

Conflict of Interest

The authors declare no conflict of interest.

Data Availability Statement

The data that support the findings of this study are available from the corresponding author upon reasonable request.

Keywords

[1] R. Kaissner, J. Li, W. Lu, X. Li, F. Neubrech, J. Wang, N. Liu, *Sci. Adv.* **2021**, *7*, eabd9450.

[2] H. Ren, X. Fang, J. Jang, J. Bürger, J. Rho, S. A. Maier, *Nat. Nanotechnol.* **2020**, *15*, 948.

[3] M. Khorasaninejad, A. Ambrosio, P. Kanhaiya, F. Capasso, *Sci. Adv.* **2016**, *2*, e1501258.

[4] L. Hüttenhofer, M. Golibrzuch, O. Bienek, F. J. Wendisch, R. Lin, M. Becherer, I. D. Sharp, S. A. Maier, E. Cortés, *Adv. Energy Mater.* **2021**, *11*, 2102877.

[5] Y. Wu, W. Yang, Y. Fan, Q. Song, S. Xiao, *Sci. Adv.* **2019**, *5*, eaax0939.

[6] A. E. Ostfeld, D. Pacifici, *Appl. Phys. Lett.* **2011**, *98*, 113112.

[7] M. Hwang, H. Lee, K. Kim, K. Jeong, S. Kwon, K. Koshelev, Y. Kivshar, H. Park, *Nat. Commun.* **2021**, *12*, 4135.

[8] X. Luyao, C. Daguan, A. C. C. Mohammad, M. L. R. J. Tatsuo, I. S., L. Xu, D. Chen, C. A. Curwen, M. Memarian, J. L. Reno, T. Itoh, B. S. Williams, *Optica* **2017**, *4*, 468.

[9] H. Altug, S. Oh, S. A. Maier, J. Homola, *Nat. Nanotechnol.* **2022**, *17*, 5.

[10] J. Wang, J. Kühne, T. Karamanos, C. Rockstuhl, S. A. Maier, A. Tittl, *Adv. Funct. Mater.* **2021**, *31*, 2104652.

[11] D. Rodrigo, A. Tittl, N. Ait-Bouziad, A. John-Herpin, O. Limaj, C. Kelly, D. Yoo, N. J. Wittenberg, S. H. Oh, H. A. Lashuel, H. Altug, *Nat. Commun.* **2018**, *9*, 2160.

[12] W. Song, X. Liang, S. Li, D. Li, K. H. L. Ramón Paniagua-Domínguez, Q. Lin, Y. Zheng, A. I. Kuznetsov, *Laser Photon. Rev.* **2021**, *15*, 2000538.

[13] J. Xiong, E. Hsiang, Z. He, T. Zhan, *Light Sci Appl* **2021**, *10*, 216.

[14] A. H. Dorrah, F. Capasso, *Science (80-.)*. **2022**, *376*, 367.

[15] Z. Qian, S. Kang, V. Rajaram, C. Cassella, N. E. Mcgruer, M. Rinaldi, *Nat. Nanotechnol.* **2017**, *12*, 969.

[16] M. Song, H. Yu, C. Hu, M. Pu, Z. Zhang, J. Luo, X. Luo, *Opt. Express* **2013**, *21*, 32207.

[17] C. Chang, W. J. M. Kort-kamp, J. Nogan, T. S. Luk, A. K. Azad, A. J. Taylor, D. A. R. Dalvit, M. Sykora, H. Chen, *Nano Lett.* **2018**, *18*, 7665.

[18] M. Diem, T. Koschny, C. M. Soukoulis, *Phys. Rev. B* **2009**, *79*, 033101.

[19] A. Lochbaum, A. Dorodnyy, U. Koch, S. M. Koep, S. Volk, Y. Fedoryshyn, V. Wood, J. Leuthold, *Nano Lett.* **2020**, *20*, 4169.

[20] T. Pohl, F. Sterl, N. Strohfeldt, H. Giessen, *ACS Sens.* **2020**, *5*, 2628.

[21] S. Kang, Z. Qian, V. Rajaram, S. D. Calisgan, A. Alù, M. Rinaldi, *Adv. Opt. Mater.* **2019**, *7*, 1801236.

[22] R. Ameling, L. Langguth, M. Hentschel, M. Mesch, P. V. Braun, *Appl. Phys. Lett.* **2010**, *97*, 253116.

[23] Z. Yong, S. Zhang, C. Gong, S. He, *Sci. Rep.* **2016**, *6*, 24063.

[24] G. Yang, S. U. Dev, M. S. Allen, W. Allen, H. Harutyunyan, *Nano Lett.* **2022**, *22*, 2001.

[25] B. I. Karawdeniya, A. M. Damry, K. Murugappan, S. Manjunath, Y. M. N. D. Y. Bandara, C. J. Jackson, D. Tricoli, D. Neshev, *Chem. Rev.* **2021**, *122*, 14990.

[26] Z. Li, S. Butun, K. Aydin, *ACS Nano* **2014**, *8*, 8242.

[27] A. Tittl, P. Mai, R. Taubert, D. Dregely, N. Liu, H. Giessen, *Nano Lett.* **2011**, *11*, 4366.

[28] J. Grant, M. Kenney, Y. D. Shah, I. Escorica-Carranza, D. R. S. Cumming, *Opt. Express* **2018**, *26*, 10408.

[29] X. Tan, H. Zhang, J. Li, H. Wan, Q. Guo, H. Zhu, H. Liu, F. Yi, *Nat. Commun.* **2020**, *11*, 5245.

[30] Z. Li, X. Sun, C. Ma, J. Li, X. Li, B. Guan, K. Chen, *Opt. Express* **2021**, *29*, 27084.

[31] B. Wang, W. Huang, L. Wang, *RSC Adv.* **2017**, *7*, 42956.

[32] L. K. Khorashad, C. Argyropoulos, *Nanophotonics* **2022**.

[33] K. Chen, R. Adato, H. Altug, *ACS Nano* **2012**, *6*, 7998.

[34] I. Hwang, J. Yu, J. Lee, J.-H. Choi, D.-G. Choi, S. Jeon, J. Lee, J.-Y. Jung, *ACS Photonics* **2018**, *5*, 3492.

[35] X. Liu, X. Jia, M. Fischer, Z. Huang, D. R. Smith, *Nano Lett.* **2018**, *18*, 6181.

[36] N. I. Landy, S. Sajuyigbe, J. J. Mock, D. R. Smith, W. J. Padilla, *Phys. Rev. Lett.* **2008**, *100*, 207402.

[37] C. Wu, B. N. Iii, G. Shvets, *Phys. Rev. B* **2011**, *84*, 075102.

[38] T. D. Dao, K. Chen, T. Nagao, *Nanoscale* **2019**, *11*, 9508.

[39] H. Tao, C. M. Bingham, A. C. Strikwerda, D. Pilon, D. Shrekenhamer, N. I. Landy, K. Fan, X. Zhang, W. J. Padilla, R. D. Averitt, *Phys. Rev. B* **2008**, *78*, 241103.

[40] R. Adato, A. Artar, S. Erramilli, H. Altug, *Nano Lett.* **2013**, *13*, 2584.

[41] M. Rybin, Y. S. L. Kivshar, *Nature* **2017**, *541*, 164.

[42] K. Koshelev, Y. Tang, K. Li, D. Choi, G. Li, Y. Kivshar, *ACS Photonics* **2019**, *6*, 1639.

[43] Y. Liang, H. Lin, K. Koshelev, F. Zhang, Y. Yang, J. Wu, Y. Kivshar, B. Jia, *Nano Lett.* **2021**, *21*, 1090.

[44] M. Qin, J. Duan, S. Xiao, W. Liu, T. Yu, T. Wang, Q. Liao, *Phys. Rev. B* **2022**, *105*, 195425.

[45] X. Wang, J. Duan, W. Chen, C. Zhou, T. Liu, S. Xiao, *Phys. Rev. B* **2020**, *102*, 155432.

[46] X. Liu, T. Tyler, T. Starr, A. F. Starr, N. M. Jokerst, W. J. Padilla, *Phys. Rev. Lett.* **2011**, *107*, 045901.

[47] A. Tittl, A. Leitis, M. Liu, F. Yesilkoy, D. Choi, D. N. Neshev, Y. S. Kivshar, H. Altug, *Science* **2018**, *360*, 1105.

[48] A. Tittl, M. G. Harats, R. Walter, X. Yin, M. Scha, *ACS Nano* **2014**, *8*, 10885.

[49] H. Chen, *Opt. Express* **2012**, *20*, 7165.

[50] L. Cong, R. Singh, *Adv. Opt. Mater.* **2019**, *7*, 1900383.

[51] F. Yesilkoy, E. R. Arvelo, Y. Jahani, M. Liu, A. Tittl, V. Cevher, Y. Kivshar, H. Altug, *Nat. Photonics* **2019**, *13*, 390.

[52] F. Ding, Y. Yang, R. A. Deshpande, S. I. Bozhevolnyi, *Nanophotonics* **2018**, *7*, 1129.

[53] J. Kühne, J. Wang, T. Weber, L. Kühner, S. A. Maier, A. Tittl, *Nanophotonics* **2021**, *10*, 4305.

[54] L. Verslegers, Z. Yu, Z. Ruan, P. B. Catrysse, S. Fan, *Phys. Rev. Lett.* **2012**, *108*, 083902.

[55] S. Li, C. Zhou, T. Liu, S. Xiao, *Phys. Rev. A* **2019**, *100*, 63803.

[56] K. Koshelev, S. Lepeshov, M. Liu, A. Bogdanov, Y. Kivshar, *Phys. Rev. Lett.* **2018**, *121*, 193903.

[57] R. L. Olmon, B. Slovick, T. W. Johnson, D. Shelton, S. H. Oh, G. D. Boreman, M. B. Raschke, *Phys. Rev. B* **2012**, *86*, 235147.

[58] D. Rodrigo, O. Limaj, D. Janner, D. Etezadi, F. J. G. D.e Abajo, V. Pruneri, H. Altug, *Science* **2015**, *349*, 165.

[59] X. Zhang, J. Qiu, J. Zhao, X. Li, L. Liu, *J. Quant. Spectrosc. Radiat. Transf.* **2020**, *252*, 107063.

[60] H. A. Haus, *Waves and Fields in Optoelectronics*, Prentice-Hall, Hoboken, NJ **1984**.